nature electronics

Article

https://doi.org/10.1038/s41928-024-01248-3

Electrical switching of the perpendicular Néel order in a collinear antiferromagnet

Received: 4 April 2023

Accepted: 16 August 2024

Published online: 30 September 2024

Check for updates

Wenqing He[1,2,7], Tianyi Zhang[1,7], Yongjian Zhou[3,7], Caihua Wan[1,4] ✉, Hao Wu[4], Baoshan Cui[4], Jihao Xia[1], Ran Zhang[1], Tengyu Guo[4], Peng Chen[1], Mingkun Zhao[1], Leina Jiang[1], Alexander Grutter[5], Purnima P. Balakrishnan[5], Andrew J. Caruana[6], Christy J. Kinane[6], Sean Langridge[6], Guoqiang Yu[1,4], Cheng Song[3] & Xiufeng Han[1,2,4] ✉

Spintronics is based on the electrical manipulation of magnetic order through current-induced spin torques. In collinear antiferromagnets with perpendicular magnetic anisotropy, binary states can be directly encoded in their opposite Néel order. The negligible stray fields and terahertz spin dynamics of these systems mean that they could potentially be used to develop ultrafast memory devices with high integration density. Here we report electrical switching of the perpendicular Néel order in a collinear antiferromagnet. We show that the Néel order in a prototypical collinear antiferromagnetic insulator—chromium oxide (Cr_2O_3)—can be switched by the spin–orbit torque with a low current density (5.8×10^6 A cm^{-2}) and read out by the anomalous Hall effect. We also show that the magnetization of a $Y_3Fe_5O_{12}$ film exchange-coupled to the Cr_2O_3 layer can be electrically switched, confirming the Néel order switching of the Cr_2O_3 layer.

Ferromagnetic (FM) spintronics is the basis of high-performance spintronic devices such as magnetic random-access memory[1–3]. This type of memory relies on magnetic tunnel junctions, which are devices with reliable resistance read out through the tunnelling magnetoresistance (TMR) effect and efficient electrical magnetic configurations written out through current-induced spin torques. In particular, spin–orbit torque (SOT) due to spin–orbit coupling in the heavy metal (HM) layer can offer efficiency, speed and flexibility[3]. Antiferromagnetic (AFM) materials could be used to improve the performance of memory devices[4–6]. The intrinsic properties of AFM materials, including zero stray field and terahertz spin dynamics[7–9], means that they could be used to create next-generation memory technologies with high density and ultrafast device operation[6,10–16].

AFM materials can be categorized as collinear or non-collinear according to their specific AFM textures. Both collinear and non-collinear AFM materials are predicted to exhibit large TMR when used in antiferromagnetic tunnel junctions (AFMTJs)[11–13]. For example, it has been predicted that the TMR ratios of AFMTJs based on collinear AFM RuO_2 are above 500%[13]. Recently, AFMTJs based on non-collinear Mn_3Pt or Mn_3Sn have been experimentally shown to exhibit a sizeable TMR effect at room temperature of 100% and 2% respectively[11,12]. Compared to non-collinear AFM materials, collinear AFM materials can offer a higher magnetic anisotropy barrier between the two memory states and, therefore, support more robust storage[4,6]. The strong exchange interactions between neighbouring magnetic moments in collinear AFM materials also lead to high spin dynamic properties and, thus, ultrafast devices[7,9]. Additionally, collinear AFM materials exhibit more uniform magnetic properties, which could streamline magnetic engineering, and efficient manipulation, which are essential for the development of all-AFM electrically controlled memory.

[1]Beijing National Laboratory for Condensed Matter Physics, Institute of Physics, Chinese Academy of Sciences, Beijing, China. [2]Center of Materials Science and Optoelectronics Engineering, University of Chinese Academy of Sciences, Beijing, China. [3]Key Laboratory of Advanced Materials (MOE), School of Materials Science and Engineering, Tsinghua University, Beijing, People's Republic of China. [4]Songshan Lake Materials Laboratory, Dongguan, China. [5]NIST Center for Neutron Research, National Institute of Standards and Technology, Gaithersburg, MD, USA. [6]ISIS Facility, STFC Rutherford Appleton Laboratory, Harwell Science and Innovation Campus, Harwell, UK. [7]These authors contributed equally: Wenqing He, Tianyi Zhang, Yongjian Zhou. ✉e-mail: wancaihua@iphy.ac.cn; xfhan@iphy.ac.cn

https://doi.org/10.1038/s41928-024-01248-3

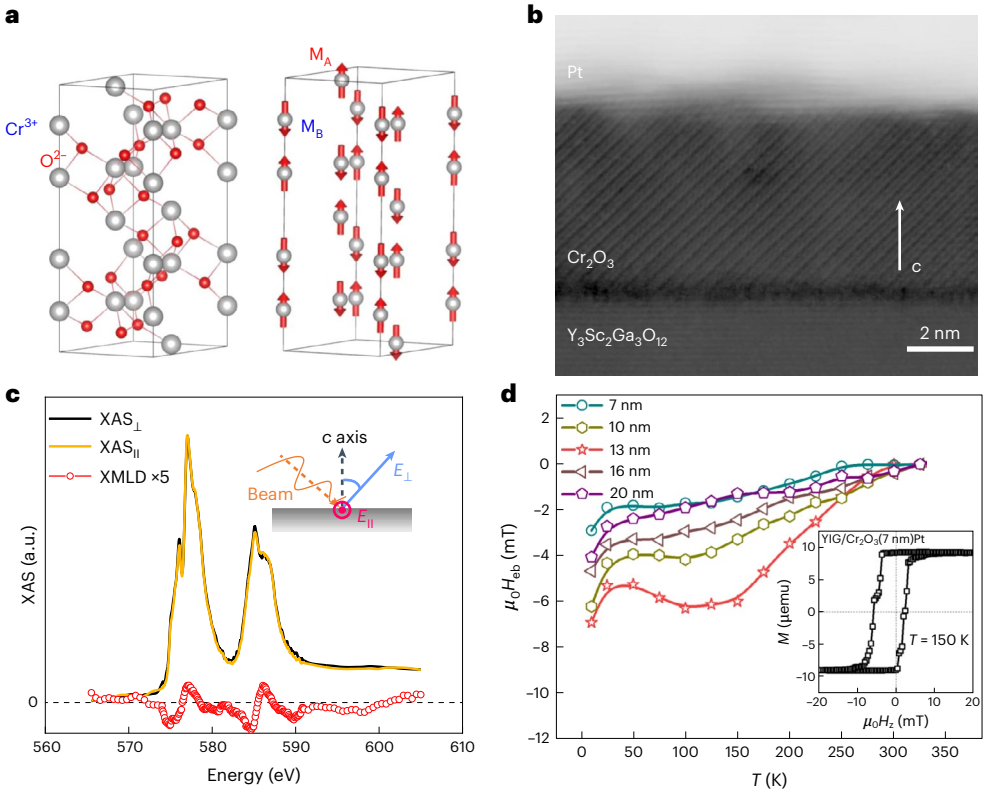

Fig. 1 | Atomic and magnetic structures of Cr_2O_3. a, Atomic and AFM structures of a Cr_2O_3 unit cell. M_A and M_B represent the sublattices of Cr_2O_3. **b**, Cross-sectional high-angle annular dark-field image of the YSGG//Cr_2O_3(7 nm)/Pt(3 nm) heterostructure. **c**, XAS and XMLD spectra of the Cr^{3+} L_3 and L_2 edges in YSGG//Cr_2O_3/Pt at 180 K, where $XAS_\parallel$ and $XAS_\perp$ denote XAS spectra recorded with different polarizations ($E_\parallel$ and $E_\perp$, which mean electron field polarization parallel and perpendicular to the surface). The polarization dependence was obtained with more than 98% linearly polarized light with an incident angle of 45° from the *c* axis. **d**, Dependence on temperature *T* of the exchange bias field H_{eb} of the samples with different Cr_2O_3 thicknesses $t_{Cr_2O_3}$. Inset, typical exchange-biased M–H_z hysteresis loop for the $t_{Cr_2O_3}$ = 7 nm sample. *M* is magnetization of YIG layer. μ_0 is vacuum magnetic permeability. a.u., arbitrary units.

Many AFM materials have several easy axes along which their Néel order can be aligned. In contrast, ferromagnets can be designed to have only two easy axes so that binary states 0 and 1 can be encoded directly[14–22]. Full switching, which refers to the rotation of a magnetic order by 180° (magnetization for FM materials and Néel order for AFM materials), can directly encode 0 and 1 binary data. Such 180° switching has several advantages over 90° or other switching strategies commonly seen in AFM memories[23,24]. First, the full switching operation maximizes the readout margin that determines the state of a device, which, in turn, reduces the time required to do so, critical for rapid operational speed. Second, 180° switching allows for a simpler device structure and, therefore, denser packaging, which further increases the storage density compared to 90°-switching-based devices. Third, the higher magnetic anisotropy barrier separating two memory states can ensure a higher retention and stronger robustness against external influences.

Non-collinear AFM metal Mn_3Sn films with tensile-strain-induced perpendicular magnetic anisotropy (PMA) from their substrates can be switched fully electrically[24]. Collinear AFM materials can be electrically switched by 90°, although there is still a debate about the specific mechanisms due to possible entanglement with electromigration and thermoelastic effects[25,26]. For applications, it is important to demonstrate 180° switching of perpendicular Néel order in a collinear AFM, which will be required for the development of ultra-dense and ultrafast AFM memory with the opposite Néel vectors as the binary states of 0 and 1.

Three characteristics are needed to clearly demonstrate 180° full switching of a collinear Néel vector: (1) a measurable anomalous Hall effect (AHE) for electrical readout, as 180° switching cannot be read out by the planar Hall effect commonly with 90° rotation; (2) PMA to distinguish influences arising from thermal and Oersted field effects and (3) Néel order switching of the collinear AFM that is distinguishable from when only uncompensated spins at the interface are switched.

In this article, we report SOT-driven full 180° switching of the Néel order in chromium oxide (Cr_2O_3). Cr_2O_3 is a collinear AFM insulator (AFI) with its easy axis along the *c* axis of a hexagonal lattice[27] (Fig. 1a). Because of its intriguing magnetoelectricity, antiferromagnetism and insulating properties[7,27–29], Cr_2O_3 is an important material for AFM magnonics[7] and multiferroics[28,29]. We detected the 180° reversal of its collinear Néel order using an AHE-like phenomenon that resulted from the interfacial spins directly coupling to the Néel order. Furthermore, we showed that the Néel order of Cr_2O_3 and the perpendicular magnetization of a $Y_3Fe_5O_{12}$ (YIG) film coupled to the Cr_2O_3 in YIG/Cr_2O_3/Pt devices can be simultaneously reversed with SOT. This confirms that the Néel vector switches by 180° throughout the entire Cr_2O_3 film and that the switching was not limited to the uncompensated interfacial spins.

Structural characterization

We grew Cr_2O_3 films with thicknesses ranging from 5 nm to 20 nm on $Y_3Sc_2Ga_3O_{12}$ (YSGG) (111) substrates using pulsed-laser deposition. A 3 nm Pt layer was then deposited on top using magnetron sputtering (Methods). M–H loops show typical field-dependent magnetization of an AFM material at different temperatures *T* (Supplementary Section I). Also visible is a tiny kink around zero field due to the uncompensated moments at the Cr_2O_3/Pt interface. Such uncompensated moments at the surface or interface in Cr_2O_3 systems have been successfully utilized to probe AFM domain walls[30], flexomagnetism and vertically graded Néel temperatures[31]. Figure 1b shows a cross-sectional image of YSGG//Cr_2O_3/Pt obtained by scanning transmission electron microscopy (TEM). The image with atomic resolution confirms the epitaxial

https://doi.org/10.1038/s41928-024-01248-3

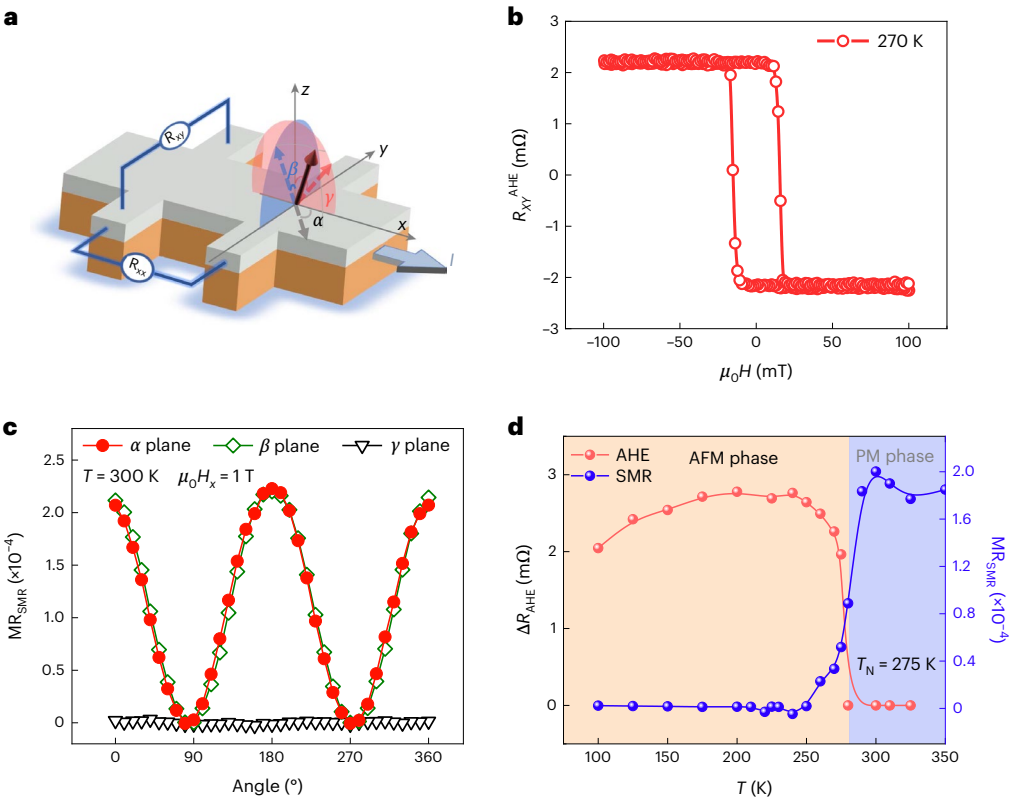

Fig. 2 | AFM ordering of Cr_2O_3 as a function of temperature. a, Measurement geometry for experimental AHE and SMR. The three angles α, β and γ are indicated. They rotate in the x–y, y–z and x–z planes, respectively. I and R_{xy} represent the current and Hall resistance. **b**, Dependence of the anomalous Hall resistance R_{xy} on the out-of-plane field H_z for the YSGG//Cr_2O_3(7)/Pt(3 nm) device. **c**, Angular dependence of the SMR ratio ($MR_{SMR} = \Delta R_{xx}/R_{xx}$) for the α, β and γ scans at 300 K under $\mu_0 H_x$ of 1 T. **d**, T dependence of ΔR_{AHE} and the SMR ratio approaches zero above 275 K, which indicates the Néel temperature T_N. The blue- and orange-shaded regions represent the PM and AFM phases, respectively.

growth of Cr_2O_3 on the YSGG substrate. Its Fourier-transformed pattern reveals that the c axis of Cr_2O_3 is out-of-plane (Supplementary Fig. 2a). The X-ray magnetic linear dichroism (XMLD) spectrum of the Cr L edge was used to characterize the Néel vector of Cr_2O_3. Figure 1c shows the data for the 7 nm Cr_2O_3 structure at 180 K. The X-ray absorption spectroscopy (XAS) spectrum is typical for Cr_2O_3, showing only the expected Cr^{3+} ions. The experimental geometry is schematically depicted in the inset of Fig. 1c. The XMLD spectrum was then obtained as $XMLD = XAS_{\parallel} - XAS_{\perp}$ (see Methods for details). It exhibits a zero–negative–positive–zero oscillating feature around the L_3 and L_2 edges, which is characteristic of a Néel vector along the out-of-plane direction[32].

Moreover, the exchange bias effect associated with the exchange coupling at the interface of FM and AFM films is further evidence for AFM order[33]. We characterized the exchange bias field in the YSGG//YIG(5 nm)/Cr_2O_3($t_{Cr_2O_3}$)/Pt(3 nm) control samples. The exchange bias field increased with an enhancement of the AFM ordering and depends on the Néel temperature T_N of the Cr_2O_3 film. We chose to grow YIG films with PMA as an exchange-biased FM material as it also grows epitaxially on YSGG and, hence, did not change the atomic structure of the Cr_2O_3 on top, as confirmed by scanning TEM (Supplementary Section II). Figure 1d shows the exchange bias field $H_{eb} \equiv (H_{c+} + H_{c-})/2$ of YSGG//YIG/Cr_2O_3 for various values of the Cr_2O_3 thickness ($t_{Cr_2O_3}$). The negative H_{eb} of all samples is non-zero below the blocking temperature, T_B, for $t_{Cr_2O_3}$ = 7 nm to 20 nm. The inset shows representative M–H_z hysteresis at 150 K. These data indicate that the AFM order was stabilized below 300 K in all samples, as expected based on the bulk compound.

AHE and T dependence of AFM ordering

We further characterized the AFM behaviour of Cr_2O_3 by magneto-transport measurements (Fig. 2). A stack with platinum thickness t_{Pt} = 3 nm was patterned into Hall bars, as shown in Fig. 2a. We measured the anomalous Hall resistance R_{xy} as a function of the out-of-plane magnetic field H_z to quantitatively estimate the AHE induced by the uncompensated spins at the Cr_2O_3/Pt interface at various temperatures. Figure 2b shows clear hysteresis in the H_z dependence of R_{xy} for $t_{Cr_2O_3}$ = 7 nm at 270 K. Figure 2d summarizes the T dependence of the remanent resistance $\Delta R_{AHE} \equiv [R_{xy}^{up} - R_{xy}^{down}]/2$ at $\mu_0 H = 0$ mT; R_{xy}^{up} and R_{xy}^{down} represent the Hall resistance as the Néel order is up and down, respectively. A ΔR_{xy} of around 0 for $T \geq 275$ K indicates a paramagnetic (PM) phase of Cr_2O_3. ΔR_{xy} increased abruptly once T was less than 275 K, and hysteresis emerged (Fig. 2b), suggesting the formation of a magnetically ordered phase. This T dependence of the AHE resistance is described well by a recent independent theoretical study in which a perpendicular surface spin state of Cr_2O_3 emerged below T_N (ref. 34). As T was decreased further, coercive field H_c increased and eventually saturated, indicating an enhanced AFM order and a PMA field H_K (Supplementary Section III). Interestingly, the AHE observed here is different from that described in ref. 35, where the AHE was attributed to non-zero parasitic magnetization due to doping. Here, in contrast, using polarized-neutron reflectometry, we confirmed that there was no parasitic magnetization inside our films (Supplementary Section IV).

Furthermore, we also measured the dependence of the longitudinal resistance ΔR_{xx} on the direction of the applied field of 1 T at different T. Current was applied along the x axis and the spin current induced by the spin Hall effect (SHE) was then polarized in the y axis. Figure 2c shows the angular dependence of ΔR_{xx} at 300 K in the PM phase. ΔR_{xx} was equal to 0 for the γ scan. The spin polarization was always perpendicular to the spins in Cr_2O_3 but oscillated with a 180° period for the α and β scans when the spins in Cr_2O_3 were driven alternatively collinear

https://doi.org/10.1038/s41928-024-01248-3

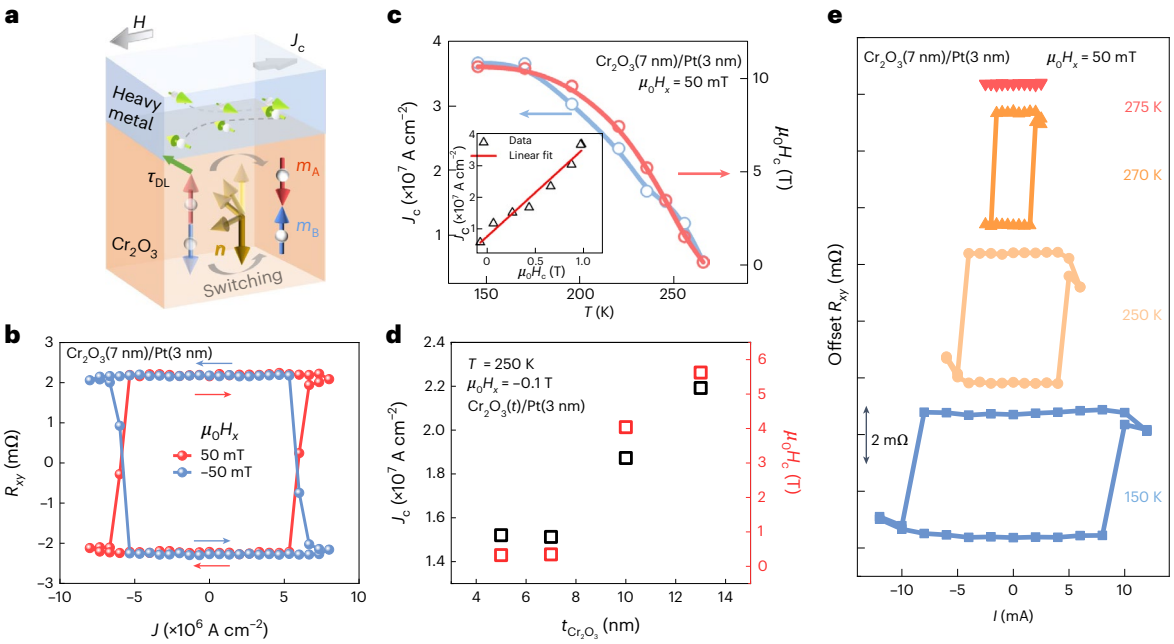

Fig. 3 | SOT-induced switching of the AFM order in Cr_2O_3/Pt bilayers. **a**, Schematic of Cr_2O_3 Néel order switching through SOT. A charge current J_c in the top Pt layer generates a SHE-induced spin current that switches the Néel order $\boldsymbol{n}$ of Cr_2O_3 by exerting an anti-damping-like torque τ_{DL} on its sublattice spins. m_A and m_B represent the sublattices of Cr_2O_3. **b**, Switching performance of the Cr_2O_3/Pt device under opposite bias fields $\mu_0H_x = \pm 50$ mT. The solid circles represent the measured Hall resistance R_{xy} when the current pulse was swept from the negative to the positive direction. **c**, T dependence of H_c and J_c of the Cr_2O_3/Pt device. **d**, Dependence of H_c and J_c on the Cr_2O_3 thickness $t_{Cr_2O_3}$ for the Cr_2O_3/Pt device. **e**, SOT-induced switching loops at different T under a bias field $\mu_0H_x = 50$ mT.

or perpendicular to the spin polarization. This observation is consistent with the spin Hall magnetoresistance (SMR) picture, thereby ruling out an anisotropic magnetoresistance origin and the magnetic proximity effect in Pt. The AHE can be explained with the SMR origin and a complex spin-mixing conductance at the Pt/Cr_2O_3 interface[36]. Figure 2d presents the T dependence of the SMR ratio ($MR_{SMR} = \Delta R_{xx}/R_{xx}$). The SMR ratio of the Cr_2O_3/Pt bilayers decreased sharply as T approached T_N, which was around 275 K, and tended to zero as T was decreased well below T_N ($T \ll T_N$) (Fig. 2d). Once the AFM order was firmly established, the applied field of 1 T was overwhelmed by H_K and could not arbitrarily rotate the spins in Cr_2O_3, so that the SMR effect was quenched in the AFM phase and arose only in the PM phase, as reported for Al_2O_3//Cr_2O_3/Pt bilayers[37]. In contrast, R_{xy} increased steeply around T_N when T was decreased. As $T > T_N$, there were no ordered interfacial spins and R_{xy} was negligibly small. Once $T \leq T_N$, the growing interfacial spins quickly gave rise to a noticeable R_{xy}, which enabled us to effectively read out the magnetic state of Cr_2O_3. The results for both SMR and AHE demonstrate an AFM to PM transition around 275 K for the 7 nm Cr_2O_3 films, consistent with the exchange bias data in Fig. 1d. Specifically, we confirmed through the temperature-dependent measurements that the AHE induced by uncompensated interfacial spins is strongly related to the bulk AFM order: the AHE vanished above T_N as determined by the SMR in Fig. 2d and the exchange bias in Fig. 1d.

Perpendicular and 180° switching of the collinear AFM order by SOT

Next, we demonstrate 180° switching of the Néel order induced by SOT in Cr_2O_3/Pt heterostructures. In the top Pt layer, a charge current generated a SHE-induced spin current that was subsequently absorbed by uncompensated spins in Cr_2O_3. The charge current exerted an anti-damping-like torque on the spins to switch their directions. Finally, the switching of the uncompensated spins brought about the switching of the Néel order of the whole Cr_2O_3 (Fig. 3a). Figure 3b shows the current-induced Néel order switching loops of Cr_2O_3 with in-plane field $\mu_0H_x = \pm 50$ mT at 270 K. We found that ΔR_{xy} at $I = 0$ mA reached 100% of the value measured in the R_{xy}–H_z curve, indicating complete switching. Moreover, the switching direction, clockwise or anticlockwise, was controlled by the sign of H_x, which is a discriminative feature of the z-type SOT switching scheme[25]. When we replaced Pt by W, which has an opposite spin Hall angle, the switching direction was also reversed (Supplementary Section V). We also replaced Pt by Cu, and no switching loop was observed (Supplementary Section V). Furthermore, we calibrated the real temperature T^* of our sample during the current pulse. The real sample temperature T^* was below T_N (Supplementary Section V). These features provide clear evidence of 180° switching of the Néel order in Cr_2O_3 driven by SOT as the dominant mechanism rather than Oersted fields or heating.

Note that the critical current $J_c = 5.8 \times 10^6$ A cm^{-2} at 270 K was lower than those reported for other non-magnetic metal/AFI systems (J_c of around 3×10^7 A cm^{-2})[20,38] (CoO or Fe_2O_3) and comparable to those reported for non-magnetic/AFM metallic systems[24]. The smaller J_c was due to the weakened uniaxial anisotropy of Cr_2O_3 as T approached T_N, as illustrated by the strong T dependence of the switching loops between 150 K and 275 K. The bipolar switching loops occurred down to 150 K but vanished at 275 K (Fig. 3e). Notably, J_c increased commensurately with H_c as T was decreased, suggesting a strong correlation with anisotropy. To test how robust the magnetic properties of collinear AFM films are against external perturbations, we investigated the SOT switching behaviour under increased H_x at lower temperature (Supplementary Fig. 7). SOT switching was achieved at $\mu_0H_x = 3$ T at 150 K, demonstrating the robustness of this switching behaviour against an external field (Supplementary Section VI). This material system can support robust binary writing, making AFM Cr_2O_3 a viable memory candidate.

To quantitatively demonstrate the role played by the uniaxial anisotropy H_K of Cr_2O_3, we systematically studied the dependence of J_c on H_x, T and $t_{Cr_2O_3}$, finding that H_K, H_c and J_c all increased as T was reduced (Fig. 3c). We also measured the switching loops for YSGG//Cr_2O_3($t_{Cr_2O_3}$)/Pt(3 nm) with $t_{Cr_2O_3}$ = 5–20 nm (Supplementary Section VII). Increasing $t_{Cr_2O_3}$ resulted in a higher H_c, especially for the thickest samples ($t_{Cr_2O_3}$ = 13 nm), which had up to 5.5 T coercivity. A further

increase in $t_{Cr_2O_3}$ led to a higher H_c beyond the limit of our equipment, so we did not obtain R_{xy}–H_z hysteresis loops for thicker samples ($t_{Cr_2O_3} > 13$ nm) below T_N. Correspondingly, J_c also increased with increasing $t_{Cr_2O_3}$. Samples with $t_{Cr_2O_3} \leq 13$ nm (Fig. 3d) showed a linear dependence on H_c and H_K. Although this linear dependence is like the z-type mode observed in HM/FM bilayers, a key difference from the HM/FM systems is that J_c was insensitive to H_x. These features were well reproduced by a theoretical model in which a much stronger AFM coupling than anisotropy was considered (Supplementary Section VIIIa). This insensitivity of the switching to an external field is beneficial in achieving strong robustness against a disturbance by an external field for memory applications.

To gain further insights into the SOT switching mechanism, we used a theoretical framework that combines a time-dependent non-equilibrium Green's function algorithm with the Landau–Lifshitz–Gilbert equation to calculate the dynamics of magnetization switching[39,40] (Supplementary Section VIIIa). Through the *s*–*d* exchange coupling, the polarized electrons exerted a torque on the localized magnetic moments at the Pt/AFM interface, which reversed the AFM Néel vector. The simulations also showed that the critical current was positively correlated with the anisotropic energy and insensitively correlated with the applied magnetic field, which is in accordance with our experiments. On the other hand, we also studied the important role of uncompensated magnetic moments on the surface during the Néel order reversal process (Supplementary Section VIIIb). The above simulations conclusively showed that differences in anisotropy, interlayer coupling and, especially, the magnetization of the interfacial region from that of the bulk Cr_2O_3 played a critical role in the field-induced and SOT-induced Néel order switching.

SOT-induced switching of the YIG/Cr_2O_3/Pt trilayer

As the Cr_2O_3 switches, we expected that SOT can also drive perpendicular magnetization switching of YIG for YSGG//YIG/Cr_2O_3/Pt samples, as interfacial coupling between YIG and Cr_2O_3 was verified and is shown in Fig. 1d. For this purpose, we first measured R_{xy} for the trilayer at different T. A sizeable R_{xy} below T_N of around 275 K confirmed the presence of the perpendicular AFM ordering (Supplementary Section IX). Next, we measured the R_{xy}–I loops to ensure that the Néel order of Cr_2O_3 in the trilayer sample could also be reversed by a current. A binary switching hysteresis was clearly observed with the reversible directions controlled by H_x, consistent with the bilayer devices, which indicates that SOT also acted effectively on the YIG/Cr_2O_3/Pt system (Fig. 4d). However, the magnetization state of YIG could not be probed by the AHE as the Pt was in proximity only to Cr_2O_3. Thus, we further conducted the in situ current-induced switching measurement using the magneto-optical Kerr effect (MOKE) for the trilayer.

Due to the negligible magnetization and transparency of Cr_2O_3, the Kerr signal can be attributed to the magnetization reversal of YIG (Fig. 4b). We successively applied positive and negative current pulses into the Hall bar channel (Fig. 4e). The observed MOKE signal for the YIG/Cr_2O_3/Pt trilayer was recorded in situ after applying the current pulses and is shown in Fig. 4f. The high and low Kerr signals closely depended on the current polarity and corresponded to the spin-up and spin-down states of YIG (Fig. 4e,f). Furthermore, the magnitude of the current-induced Kerr signal change in Fig. 4f is in agreement with that of the field-induced YIG layer switching shown in Fig. 4b, indicating full switching of the YIG magnetization. Both magnetization states of YIG can be reproducibly written. To further verify that the alternating Kerr signals originated from SOT-induced switching of the YIG magnetization, we changed the H_x direction. As a result, the polarity of the MOKE signal was also reversed (Fig. 4f). When the current was switched off, the final state was maintained, confirming its non-volatility (the green region in Fig. 4f). We also reduced our measurement temperature to 175 K and repeated the measurements, achieving the same results. In the control experiment, we also applied the alternating current pulses to the Cr_2O_3/Pt bilayer sample. No Kerr signal switching was observed (Fig. 4g). The magnetization switching of the YIG layer, which was not in direct contact with Pt, demonstrates the switching of the entire Néel vector of Cr_2O_3, and it cannot be explained by the switching of the interfacial uncompensated spins at the Cr_2O_3/Pt interface. Because the exchange coupling energy is smaller (larger) than the anisotropy energy of Cr_2O_3 (PMA of YIG) for the YIG/Cr_2O_3/Pt trilayer, the magnetization of YIG and the Néel vector of Cr_2O_3 can be independently switched by a magnetic field. However, because of the direct contact between Pt and Cr_2O_3 and because the SOT is imposed only on the first layer of the Cr_2O_3, the magnetization switching of YIG was cascaded by the Néel vector switching of Cr_2O_3. Thus, they were observed to simultaneously switch in the current-switching experiment.

Note that several AFM-based magnon-transfer torque (MTT) effects have recently been reported to enable FM magnetization switching in FM/AFI/HM systems[41,42]. In this scenario, spin accumulation at the HM/AFI interfaces generates or annihilates magnons inside the AFI and, thus, drives a magnon current across the AFI to deliver spin-angular momenta and eventually reverse the magnetization of the ferromagnetism by the spin torque transferred at the FM/AFI interface. In this process, the spin polarization must be collinear with the Néel vector of the AFI, as is required for magnon generation or annihilation[43,44]. In contrast, here, the spin polarization was perpendicular to the Néel vector of Cr_2O_3, making the MTT effect impossible. Thus, we propose that the magnetization switching of YIG is mediated by the switching of the Cr_2O_3 Néel vector rather than a magnon current.

To experimentally rule out the MTT mechanism, we measured the SMR of a YIG/Cr_2O_3/Pt trilayer. If the MTT were dominant, the YIG layer would absorb the magnon current at the YIG/Cr_2O_3 interface so that the YIG magnetization should have influenced the Pt resistance according to the SMR mechanism. However, no SMR was observed below T_N for the trilayer (Supplementary Section X), indicating that the spin current produced in Pt has already been fully absorbed by Cr_2O_3 before reaching the YIG layer. The T dependence of SMR is consistent with the experimental data in ref. 45. These observations strongly favour a picture in which the spin torque transferred from Pt is directly imposed on the perpendicular Néel vector of Cr_2O_3, resulting in 180° switching of its Néel order and indirectly reversing the YIG magnetization through exchange coupling with Cr_2O_3 (Fig. 4a).

Thus, our experiment shows that AFM-mediated torque is a pathway for energy-efficient magnetization switching of magnetic insulators. This process is as energy efficient as MTT. Such a picture is also well reproduced by theoretical calculations, which revealed that the Cr_2O_3 Néel vector and YIG magnetization are simultaneously switched by a polarized spin current (Supplementary Section VIIIa). In addition, the AFM-mediated torque mechanism, which can non-locally switch the magnetization of a magnetic insulator embedded in AFMI/FM heterostructures, could potentially be used to electrically control the magnetic states of emerging insulating magnon devices, such as magnon junctions[46,47].

From the above observations and analysis, it is clear that this magnetic insulator/AFI/HM trilayer system with perpendicular anisotropy is required to unambiguously demonstrate the 180° SOT switching of the AFM Néel order. There is no physical limitation to prevent the same mechanism from being generalized to other collinear AFM systems, such as metallic MnN (ref. 48), FeRh (ref. 49), Mn_5Si_3, CrSb, RuO_2 (ref. 13) and so on. It has been predicted that for some of these materials, for example RuO_2, they could potentially develop AFMTJs with ultrahigh TMR ratios of above 500% (ref. 13).

The performance of electrical manipulation of the AFM order is crucial for practical memory devices. More specifically, the spin current generated by subterahertz AFM resonance has been reported in Cr_2O_3, which offers attractive dynamic properties for potential applications in ultrafast devices. Accordingly, we also switched the Néel vector of

https://doi.org/10.1038/s41928-024-01248-3

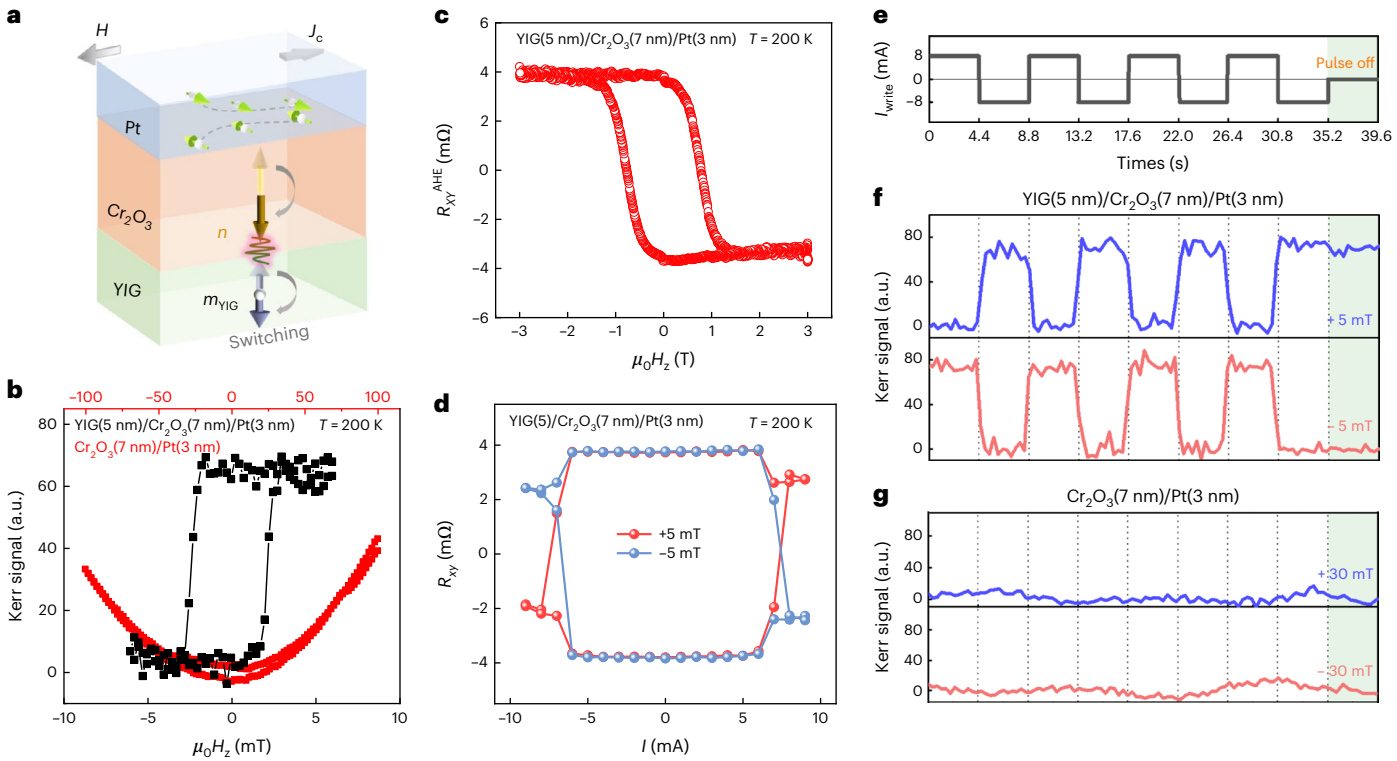

Fig. 4 | SOT-induced switching of the YIG/Cr_2O_3/Pt trilayer. a, Schematic of AFM-mediated switching for the YIG/Cr_2O_3/Pt trilayer. A charge current J_c in the top Pt layer generates a SHE-induced spin current that switches the Néel order (n) of Cr_2O_3 by SOT. Simultaneously, the bottom YIG layer m_{YIG} switches due to interfacial exchange coupling at the YIG/Cr_2O_3 interface. **b**, Magnetization loop detected by MOKE for the YIG/Cr_2O_3/Pt trilayer. No hysteretic MOKE signal was obtained for the Cr_2O_3/Pt bilayer. **c**, Dependence of the anomalous Hall resistance of the trilayer on H_z. **d**, Current-induced R_{xy} switching of the trilayer. The switching direction depends on the collinear field of the current. **e**, Write current pulse sequence I_{write} over time. The green region indicates that the current pulse is switched off. **f**, States observed by the MOKE signal after each current pulse in **e**. The switching of the YIG magnetization was consistent with reversed switching directions at ±5 mT. **g**, No switching signal was detected for the Cr_2O_3/Pt bilayer.

Cr_2O_3 using 6 ns current pulses as a step towards ultrafast and robust device applications[7] (Supplementary Section XI). Furthermore, the endurance of the performance of SOT switching was tested through the application of 5,000 alternating pulse currents. The switching curves obtained did not show noticeable degradation, demonstrating high endurance (Supplementary Section XII). Note that T_N for Cr_2O_3 is, at present, 275 K, which is insufficient for room-temperature applications. However, epitaxial or chemical strain engineering could be a path towards increasing T_N to 400 K (refs. 31,50,51), which would render Cr_2O_3 relevant for industrial microelectronics applications.

Conclusions

We have reported efficient control over the Néel order of the collinear AFI Cr_2O_3 with PMA by SOT. The AFM order was switched with a minimum current density of around 5.8×10^6 A cm^{-2}. Furthermore, we showed endurance over 2,500 write cycles and high-speed switching driven by 6 ns pulses. With both SOT-writing and reliable AHE readout, the collinear and perpendicular AFM Cr_2O_3 is a promising candidate for AFM memories with fully electrical operation, low-energy consumption, high density, ultrafast speed and strong robustness against disturbance.

Methods

Sample and device fabrication

High-quality Cr_2O_3 layers with different thicknesses were prepared by pulsed-laser deposition with a KrF excimer laser. The YSGG substrate temperature was kept at 723 K and the O_2 pressure was 20 mTorr (1 Torr is equal to 133.3 Pa) during deposition. The deposition rate of Cr_2O_3 was around 0.5 nm min^{-1}. Then the samples were transported to the magnetron sputtering system, which deposited a Pt or W layer (3 nm) on the Cr_2O_3 at room temperature. For YIG/Cr_2O_3/Pt trilayer samples, we first grew a 5-nm-thick single-crystalline YIG layer on (111)-oriented YSGG substrates using magnetron sputtering, which was annealed at 800 °C for 1 h. Subsequently, Cr_2O_3 and Pt were grown as described above.

Structural analysis was performed by high-resolution TEM. The cross-sectional TEM image of Cr_2O_3/Pt and YIG/Cr_2O_3/Pt samples revealed high-quality Cr_2O_3 and YIG layers, which laid the foundation for the transport and switching measurements. The Fourier transformation of the high-resolution TEM images of Cr_2O_3/Pt and YIG/Cr_2O_3/Pt samples showed the same epitaxial relationship, that is, (0006)-oriented Cr_2O_3 had been grown epitaxially on (111)-oriented YSGG (YIG).

Magnetization measurements were carried out in a commercial superconducting quantum interference device magnetometer (MPMS3, Quantum Design). To obtain the signal from only the multilayers, the diamagnetic contribution of the YSGG substrate was separately measured and subtracted from the total M. The Cr_2O_3 magnetization loops are shown as a function of out-of-plane magnetic field within ±4 T at 100 and 300 K in the Supplementary Information. For the YIG/Cr_2O_3/Pt trilayer samples, we first carried out a field cooling process and then measured M–H loops to obtain the exchange bias field at different temperatures. The exchange bias field H_{eb} of YSGG//YIG/Cr_2O_3 for various $t_{Cr_2O_3}$ is shown in Fig. 1d. The XAS and XMLD measurements were performed by a vector magnetic system in one of the BL07U end stations at the Shanghai Synchrotron Radiation Facility for a sample of YSGG//Cr_2O_3(7 nm)/Pt(1 nm) at 180 K, which was below T_N. The polarization dependence was obtained with linearly polarized light with an incident

angle of 45° from the *c* axis, which yielded near $E_{\perp}$ or $E_{\parallel}$ in a fixed experimental geometry by utilizing the planar or vertical polarization selectivity of the elliptically polarized undulator. The XMLD spectra were obtained by subtracting $E_{\perp}$ from the $E_{\parallel}$ spectra. For the transport and switching measurements, the multilayers were patterned into Hall bar devices with in-plane dimensions of 10 μm × 100 μm using standard photolithography combined with an Ar^{+} etching process, and Pt/Au contact pads and wires were deposited by magnetron sputtering.

Polarized-neutron reflectometry measurements

The polarized-neutron reflectometry measurements were performed using the POLREF instrument at the ISIS neutron and muon source. The POLREF beamline is a white-beam time-of-flight polarized-neutron reflectometer with a polarized wavelength band of 0.2–1.4 nm. The samples were mounted horizontally in a helium flow cryostat within an electromagnet with a maximum field of ±700 mT, which could be applied in the plane of the sample. A helium exchange gas pressure of 4 kPa was used, providing a temperature stability of ±0.01 K. The samples were held in place by gravity alone to avoid the use of epoxy, which may have strained the film or substrates upon cooling to lower temperatures. The data were reduced using the Mantid framework in combination with in-house Python scripts and analysed using the Refl1D software package. Uncertainties on fitted parameters were obtained using the DREAM algorithm in the Bumps software package, a Markov-chain Monte Carlo method.

Transport measurements

The transport characteristics were measured by a standard four-probe method using a physical property measurement system (Quantum Design). First, we measured the transverse resistance R_{xy} as a function of H_z to obtain the anomalous Hall resistance. After subtracting the linear background due to the ordinary Hall effect, clear hysteresis was observed when T was far below 275 K. For the SMR measurement, we measured the longitudinal resistance R_{xx} after rotating the devices in the α, β and γ planes. For the switching measurement, we applied a 100 ms pulse write current I_{write} to switch the AFM domains. Then a d.c. read current I_{read} = 0.1 mA was applied along the x direction. A wait time of 500 ms was inserted after turning off the write current and before measuring R_{xy}. Room-temperature measurements were carried out at the 3D Magnetic Field Probe Station, East Changing Technologies, China.

MOKE measurements

For the YIG layer switching experiments, we used a magneto-optic Kerr microscope (Evico), which facilitated the visualization of the magnetization switching processes as well as optically recording the magnetization curves for the magnetic materials. The MOKE system was also equipped with an external electrical measurement system, which included a Keithley 6221 source meter and a Keithley 2182 source meter to provide the currents and measure the Hall voltage, respectively. We first measured the magnetization curves of YSGG//Cr_2O_3(7 nm)/Pt(3 nm) and YSGG//YIG(5)/Cr_2O_3(7 nm)/Pt(3 nm) samples dependent on the out-of-plane magnetic field at 200 K. The obvious magnetization curves were observed in trilayer samples but vanished in bilayer samples, manifesting the PMA of YIG and the negligible magnetization of Cr_2O_3. Note that no clear change of the MOKE image was observed by MOKE microscopy after YIG magnetization switching, which may be caused by the thinner YIG layer in combination with the weak magnetization. We used a time-resolved-MOKE model to investigate the magnetization dynamics of a YIG layer during SOT switching. In the current-switching experiment, a Keithley 2612B source meter was used to apply current pulses with a pulse length of 1 ms through the devices, and the magnetization states were captured as Kerr signals using a Kerr microscope at the same time. The measurement sequence with different in-plane H_x values is shown in Fig. 4.

Data availability

The data that support the findings of this study are available from the corresponding authors upon reasonable request.

Code availability

The codes that support the theoretical modelling of this study are available from the corresponding authors upon reasonable request.

References

1. Liu, L. Q. et al. Spin-torque switching with the giant spin Hall effect of tantalum. *Science* **336**, 555–558 (2012).
2. Miron, I. M. et al. Perpendicular switching of a single ferromagnetic layer induced by in-plane current injection. *Nature* **476**, 189–193 (2011).
3. He, W. et al. Field-free spin-orbit torque switching enabled by the interlayer Dzyaloshinskii-Moriya interaction. *Nano Lett.* **22**, 6857–6865 (2022).
4. Jungwirth, T. et al. Antiferromagnetic spintronics. *Nat. Nanotechnol.* **11**, 231–241 (2016).
5. Wadley, P. et al. Electrical switching of an antiferromagnet. *Science* **351**, 587–590 (2016).
6. Baltz, V. et al. Antiferromagnetic spintronics. *Rev. Mod. Phys.* **90**, 015005 (2018).
7. Li, J. et al. Spin current from sub-terahertz-generated antiferromagnetic magnons. *Nature* **578**, 70–74 (2020).
8. Keffer, F. & Kittel, C. Theory of antiferromagnetic resonance. *Phys. Rev.* **85**, 329–337 (1952).
9. Cheng, R. et al. Terahertz antiferromagnetic spin Hall nano-oscillator. *Phys. Rev. Lett.* **116**, 207603 (2016).
10. Šmejkal, L. et al. Anomalous Hall antiferromagnets. *Nat. Rev. Mater.* **7**, 482–496 (2022).
11. Qin, P. et al. Room-temperature magnetoresistance in an all-antiferromagnetic tunnel junction. *Nature* **613**, 485–489 (2023).
12. Chen, X. et al. Octupole-driven magnetoresistance in an antiferromagnetic tunnel junction. *Nature* **613**, 490–495 (2023).
13. Shao, D. F., Zhang, S. H., Li, M., Eom, C. B. & Tsymbal, E. Y. Spin-neutral currents for spintronics. *Nat. Commun.* **12**, 7061 (2021).
14. Banabir, P. et al. Setting of the magnetic structure of chiral kagome antiferromagnets by a seeded spin-orbit torque. *Sci. Adv.* **8**, eabo5930 (2022).
15. Krishnaswamy, G. K. et al. Time-dependent multistate switching of topological antiferromagnetic order in Mn_3Sn. *Phys. Rev. Appl.* **18**, 024064 (2022).
16. Yan, G. Q. et al. Quantum sensing and imaging of spin-orbit-torque-driven spin dynamics in the non-collinear antiferromagnet Mn_3Sn. *Adv. Mater.* **34**, e2200327 (2022).
17. Tsai, H. et al. Electrical manipulation of a topological antiferromagnetic state. *Nature* **580**, 608–613 (2020).
18. Takeuchi, Y. et al. Chiral-spin rotation of non-collinear antiferromagnet by spin-orbit torque. *Nat. Mater.* **20**, 1364–1370 (2021).
19. Chen, X. et al. Electric field control of Neel spin-orbit torque in an antiferromagnet. *Nat. Mater.* **18**, 931–935 (2019).
20. Bodnar, S. Y. et al. Writing and reading antiferromagnetic Mn_2Au by Neel spin-orbit torques and large anisotropic magnetoresistance. *Nat. Commun.* **9**, 348 (2018).
21. Chen, X. Z. et al. Antidamping-torque-induced switching in biaxial antiferromagnetic insulators. *Phys. Rev. Lett.* **120**, 207204 (2018).
22. Zhang, P. et al. Control of Neel vector with spin-orbit torques in an antiferromagnetic insulator with tilted easy plane. *Phys. Rev. Lett.* **129**, 017203 (2022).
23. Kim, K.-J. et al. Strain solves switch hitch for magnetic material. *Nature* **607**, 452–453 (2022).

24. Higo, T. et al. Perpendicular full switching of chiral antiferromagnetic order by current. *Nature* **607**, 474–479 (2022).
25. Zhang, P. et al. Quantitative study on current-induced effect in an antiferromagnet insulator/Pt bilayer film. *Phys. Rev. Lett.* **123**, 247206 (2019).
26. Chiang, C. C. et al. Absence of evidence of electrical switching of the antiferromagnetic Neel vector. *Phys. Rev. Lett.* **123**, 227203 (2019).
27. Qiu, Z. et al. Spin colossal magnetoresistance in an antiferromagnetic insulator. *Nat. Mater.* **17**, 577–580 (2018).
28. Kosub, T. et al. Purely antiferromagnetic magnetoelectric random access memory. *Nat. Commun.* **8**, 13985 (2017).
29. He, X. et al. Robust isothermal electric control of exchange bias at room temperature. *Nat. Mater.* **9**, 579–585 (2010).
30. Hedrich, N. et al. Nanoscale mechanics of antiferromagnetic domain walls. *Nat. Phys.* **17**, 574–577 (2021).
31. Makushko, P. et al. Flexomagnetism and vertically graded Neel temperature of antiferromagnetic Cr_2O_3 thin films. *Nat. Commun.* **13**, 6745 (2022).
32. Park, J. et al. Thickness driven spin reorientation transition of epitaxial $LaCrO_3$ films. *Appl. Phys. Lett.* **112**, 1112403 (2018).
33. Nogués, J. et al. Exchange bias. *J. Magn. Magn. Mater.* **192**, 203–232 (1999).
34. Sophie F. W. et al. Characterizing and overcoming surface paramagnetism in magnetoelectric antiferromagnets. *Phys. Rev. Lett.* **130**, 146701 (2022).
35. Nozaki, T. et al. Manipulation of antiferromagnetic spin using tunable parasitic magnetization in magnetoelectric antiferromagnet. *Phys. Status Solidi Rapid Res. Lett.* https://doi.org/10.1002/pssr.201800366 (2018).
36. Chen, Y.-T. et al. Theory of spin Hall magnetoresistance. *Phys. Rev. B* **87**, 144411 (2013).
37. Schlitz, R. et al. Evolution of the spin Hall magnetoresistance in Cr_2O_3/Pt bilayers close to the Néel temperature. *Appl. Phys. Lett.* **112**, 132401 (2018).
38. Baldrati, L. et al. Efficient spin torques in antiferromagnetic CoO/Pt quantified by comparing field- and current-induced switching. *Phys. Rev. Lett.* **125**, 077201 (2020).
39. Suresh, A. et al. Magnon- versus electron-mediated spin-transfer torque exerted by spin current across an antiferromagnetic insulator to switch the magnetization of an adjacent ferromagnetic metal. *Phys. Rev. Appl.* **15**, 034089 (2021).
40. Petrović, M. D. et al. Spin and charge pumping by a steady or pulse-current-driven magnetic domain wall: a self-consistent multiscale time-dependent quantum-classical hybrid approach. *Phys. Rev. Appl.* **10**, 054038 (2018).
41. Wang, Y. et al. Magnetization switching by magnon-mediated spin torque through an antiferromagnetic insulator. *Science* **366**, 1125–1128 (2019).
42. Guo, C. Y. et al. Switching the perpendicular magnetization of a magnetic insulator by magnon transfer torque. *Phys. Rev. B* **104**, 094412 (2021).
43. Zhang, S. S. L. & Zhang, S. F. Magnon mediated electric current drag across a ferromagnetic insulator layer. *Phys. Rev. Lett.* **109**, 096603 (2012).
44. Cornelissen, L. J., Liu, J., Duine, R. A., Youssef, J. B. & van Wees, B. J. Long-distance transport of magnon spin information in a magnetic insulator at room temperature. *Nat. Phys.* **11**, 1022–1026 (2015).
45. Qin, J. et al. Spin Hall magnetoresistance in Pt/Cr_2O_3/YIG structure. *J. Magn. Magn. Mater.* **534**, 167980 (2021).
46. Lee, J. et al. Antiferromagnetic spin orientation and magnetic domain structure in epitaxially grown MnN studied using optical second-harmonic generation. *Phys. Rev. Appl.* **18**, 034020 (2022).
47. Ju, G. et al. Ultrafast generation of ferromagnetic order via a laser-induced phase transformation in FeRh thin films. *Phys. Rev. Lett.* **93**, 197403 (2004).
48. Guo, C. Y. et al. A nonlocal spin Hall magnetoresistance in a platinum layer deposited on a magnon junction. *Nat. Electron.* **3**, 304–308 (2020).
49. He, W. et al. Magnon junction effect in $Y_3Fe_5O_{12}$/CoO/$Y_3Fe_5O_{12}$ insulating heterostructures. *Appl. Phys. Lett.* **119**, 212410 (2021).
50. Kota, Y. et al. Strain-induced Néel temperature enhancement in corundum-type Cr_2O_3 and Fe_2O_3. *Appl. Phys. Express* **6**, 113007 (2013).
51. Wang, X., Ujimoto, K., Toyoki, K., Nakatani, R. & Shiratsuchi, Y. Increase of Néel temperature of magnetoelectric Cr_2O_3 thin film by epitaxial lattice matching. *Appl. Phys. Lett.* **121**, 182402 (2022).

Acknowledgements

The XMLD measurements were carried out at the BL07U beamline of the Shanghai Synchrotron Radiation Facility. We appreciate the financial support from the National Key Research and Development Program of China (MOST; Grant Nos. 2022YFA1402800 and 2022YFA1402603), the National Natural Science Foundation of China (Grant Nos. 51831012, 12134017, 11974398 and 52161160334) and the Strategic Priority Research Programme B of the Chinese Academy of Sciences (Grant No. XDB33000000). C.H.W. appreciates the financial support from the Youth Innovation Promotion Association, Chinese Academy of Sciences (Grant No. 2020008). We thank the ISIS Neutron and Muon Source for the provision of neutron beam time (RB2220260). Certain commercial equipment, instruments, software or materials are identified in this paper to specify the experimental procedure adequately. Such identifications are not intended to imply recommendation or endorsement by the National Institute of Standards and Technology, nor are they intended to imply that the materials or equipment identified are necessarily the best available for the purpose.

Author contributions

X.F.H. led and was involved in all aspects of the project. W.Q.H., Y.J.Z. and C.S. deposited stacks and fabricated devices. W.Q.H. and C.H.W. measured the magnetic and transport properties. W.Q.H. performed the MOKE measurements with assistance from B.S.C., G.Q.Y. and T.Y.G. T.Y.Z., C.H.W. and W.Q.H. contributed to the modelling and theoretical analysis. W.Q.H. and J.H.X. conducted the XAS and XMLD experiment at the Shanghai Synchrotron Radiation Facility. A.J.C., P.P.B., C.J.K., A.G., S.L. and H.W. conducted the polarized-neutron scattering experiments at the ISIS facility. P.C., R.Z., M.K.Z. and L.N.J. analysed the TEM data. W.Q.H., C.H.W. and X.F.H. wrote the paper. X.F.H. and C.H.W. supervised and designed the experiments. All authors contributed to the data analysis.

Competing interests

The authors declare no competing interests.

Additional information

Supplementary information The online version contains supplementary material available at https://doi.org/10.1038/s41928-024-01248-3.

Correspondence and requests for materials should be addressed to Caihua Wan or Xiufeng Han.

Peer review information *Nature Electronics* thanks Kyung-Jin Lee and the other, anonymous, reviewer(s) for their contribution to the peer review of this work.

Reprints and permissions information is available at www.nature.com/reprints.

Publisher's note Springer Nature remains neutral with regard to jurisdictional claims in published maps and institutional affiliations.

Springer Nature or its licensor (e.g. a society or other partner) holds exclusive rights to this article under a publishing agreement with the author(s) or other rightsholder(s); author self-archiving of the accepted manuscript version of this article is solely governed by the terms of such publishing agreement and applicable law.

© The Author(s), under exclusive licence to Springer Nature Limited 2024